

# A G space theory and a weakened weak ( $W^2$ ) form for a unified formulation of compatible and incompatible methods: Part II applications to solid mechanics problems

G. R. Liu<sup>1,2,\*</sup>, †

<sup>1</sup>*Centre for Advanced Computations in Engineering Science, Department of Mechanical Engineering, National University of Singapore, 9 Engineering Drive 1, Singapore 117576, Singapore*

<sup>2</sup>*Singapore—MIT Alliance (SMA), E4-04-10, 4 Engineering Drive 3 Singapore, 117576, Singapore*

## SUMMARY

In part I of this paper, we have established the G space theory and fundamentals for  $W^2$  formulation. Part II focuses on the applications of the G space theory to formulate  $W^2$  models for solid mechanics problems. We first define a bilinear form, prove some of the important properties, and prove that the  $W^2$  formulation will be spatially stable, and convergent to exact solutions. We then present examples of some of the possible  $W^2$  models including the SFEM, NS-FEM, ES-FEM, NS-PIM, ES-PIM, and CS-PIM. We show the major properties of these models: (1) they are variationally consistent in a conventional sense, if the solution is sought in a proper H space (compatible cases); (2) They pass the standard patch test when the solution is sought in a proper G space with discontinuous functions (incompatible cases); (3) the stiffness of the discretized model is reduced compared with the finite element method (FEM) model and possibly to the exact model, allowing us to obtain upper bound solutions with respect to both the FEM and the exact solutions and (4) the  $W^2$  models are less sensitive to the quality of the mesh, and triangular meshes can be used without any accuracy problems. These properties and theories have been confirmed numerically via examples solved using a number of  $W^2$  models including compatible and incompatible cases. We shall see that the G space theory and the  $W^2$  forms can formulate a variety of stable and convergent numerical methods with the FEM as one special case. Copyright © 2009 John Wiley & Sons, Ltd.

Received 17 July 2008; Revised 6 June 2009; Accepted 23 June 2009

**KEY WORDS:** numerical method; meshfree method; G space; weakened weakform; point interpolation method; finite element method; solution bound; variational principle; Galerkin weak form; compatibility

\*Correspondence to: G. R. Liu, Centre for Advanced Computations in Engineering Science, Department of Mechanical Engineering, National University of Singapore, 9 Engineering Drive 1, Singapore 117576, Singapore.

†E-mail: mpeliugr@nus.edu.sg

Contract/grant sponsor: A\*STAR, Singapore

Contract/grant sponsor: Open Research Fund Program of the State Key Laboratory of Advanced Technology of Design and Manufacturing for Vehicle Body, Hunan University; contract/grant number: 40915001

## 1. INTRODUCTION

In part I of this paper the theory and fundamentals for  $W^2$  formulations have been established [1]. It is proven that a numerical method developed based on the  $W^2$  formulation will be spatially stable and converge, as long as the original physical problem is well-posed. The theory is applicable to any problems to which the standard weak formulation is applicable, and offers numerical solutions with special properties including softened behavior, upper bounds, and ultra accuracy. In part II of this paper, we focus on the application of the theory to formulate various  $W^2$  models. We first define a bilinear form, prove some of the important general properties of the bilinear form including a set of key inequalities, and prove that the  $W^2$  formulation will be spatially stable and convergent to exact solutions. A class of effective numerical methods, including element-based and meshfree methods, is established that possess some desired superior properties: the SFEM, NS-FEM, ES-FEM, NS-PIM, ES-PIM, and CS-PIM.

The numerical methods developed based on the  $W^2$  form will possess three major important properties: (1) they are variationally consistent in a conventional sense, if the solution is sought in a proper  $H$  space (compatible cases); (2) they pass the standard patch test when the solution is sought in a proper  $G$  space with discontinuous functions (incompatible cases); (3) the stiffness of the discretized model will be reduced compared with the finite element method (FEM) model and possibly to the exact model, which allows us to obtain upper bound solutions with respect to both the FEM and the exact solutions; and (4) the  $W^2$  models are less sensitive to the quality of the mesh, and triangular meshes can be used without any accuracy problems. These properties have been confirmed numerically via examples solved using a number of  $W^2$  models including the node-based smoothed point interpolation method (NS-PIM [2, 3]), PIMs using radial basis functions such as NS-RPIM [4], node-based smoothed finite element method (NS-FEM [5]), edge-based smoothed FEM (ES-FEM) for 2D problems [6] and face-based smoothed FEM (FS-FEM) for 3D problems [7], the smoothed finite element method (SFEM [8, 9]), and some newly formulated models of edge-based smoothed PIM (ES-PIM), ES-RPIM, CS-PIM, and CS-RPIM.

## 2. BRIEF ON WEAK FORMULATION

Consider solid mechanics problems of linear elasticity, the strong form of partial differential equations (PDEs) with boundary conditions, found in [10]. In this work, we consider only solids of stable materials defined by the following remark.

### *Remark 2.1*

*Stable materials:* A material is *mechanically stable*, if any finite amount of strains will result in a finite amount of stresses and vice versa, and hence a *finite* positive amount of strain energy. In other words, these material constants are positive definite or the matrix of the material constants is symmetric positive definite or SPD.

### *2.1. Weak form statement*

Assuming that the solid occupies a physical domain of  $\Omega \in \mathfrak{R}^d$  (where  $d$  is the dimension of domain) bounded by  $\Gamma$  that is ‘*Lipschitzian*’. The standard weak formulation for linear elasticity problems (see, e.g. [11]) can be summarized as follows. By multiplying the equilibrium equations

with a test function  $v \in \mathbb{S} \subset (\mathbb{H}_0^1(\Omega))^d$  and performing integration over the problem domain  $\Omega$ , we have

$$\int_{\Omega} v_i \frac{\partial \sigma_{ij}}{\partial x_j} d\Omega + \int_{\Omega} b_i v_i d\Omega = 0, \quad v \in \mathbb{S} \tag{1}$$

where  $i, j = 1, \dots, d$ . Applying Green divergence theorem yields

$$\int_{\Omega} \frac{\partial v_i}{\partial x_j} \sigma_{ij} d\Omega - \int_{\Gamma_N} v_i \sigma_{ij} n_j d\Gamma - \int_{\Omega} b_i v_i d\Omega = 0 \tag{2}$$

Applying now the boundary conditions to the above equation leads to

$$\underbrace{\int_{\Omega} \frac{\partial v_i}{\partial x_j} \left( C_{ijkl} \frac{\partial u_k}{\partial x_l} \right) d\Omega}_{a(u,v)} = \underbrace{\int_{\Gamma_N} v_i \sigma_{ij} n_j d\Gamma + \int_{\Omega} b_i v_i d\Omega}_{f(v)} \tag{3}$$

We now have the well-known bilinear form:

$$a(w, v) = \int_{\Omega} \frac{\partial v_i}{\partial x_j} \left( C_{ijkl} \frac{\partial w_k}{\partial x_l} \right) d\Omega \tag{4}$$

where  $v, w \in \mathbb{S}$  that has basic properties of symmetry and positivity and the ellipticity: meaning that for solids of stable materials (see Remark 2.1) there exists a positive constant  $c$  such that

$$a(w, w) \geq c \|w\|_{H^1(\Omega)}^2 \quad \forall w \in \mathbb{S} \tag{5}$$

The above inequality is rooted in the fact that the semi norm  $H^1$  norm is equivalent to the full  $H^1$  norm, meaning that there exists a positive constant  $c_{PF}$  such that

$$c_{PF} \|w\|_{H^1(\Omega)}^2 \leq |w|_{H^1(\Omega)}^2 \quad \forall w \in \mathbb{S} \tag{6}$$

which is known as the Poincare–Friedrichs inequality and  $c_{PF}$  is known as the Poincare–Friedrichs constant. The Poincare–Friedrichs inequality is one of the most important inequalities in weak formulation, because it ensures fundamentally the stability of the weak form formulation. The linear functional

$$f(v) = \int_{\Gamma_N} v_i t_i d\Gamma + \int_{\Omega} b_i v_i d\Omega \tag{7}$$

It follows from Equation (3) that the exact solution of the displacement  $u \in \mathbb{S}$  satisfies

$$a(u, v) = f(v) \quad \forall v \in \mathbb{S} \tag{8}$$

where  $u$  is the ‘exact’ displacement field of a given problem that satisfies the strong form. We make now the following remark for future references.

*Remark 2.2*

Weak formulation: From Equation (4), we observe that we need only first derivatives for all functions involved in the formulation. This is because the part of the 2nd order derivatives on

$u$  in the strong form has been ‘transferred’ to the so-called test function  $v$ . As a result the continuity requirements on both functions  $u$  and  $v$  are *weakened*: they all need to be only 1st order differentiable, compared with the requirement of 2nd order differentiable in the strong formulation [10]. Both functions  $u$  and  $v$  can live in a Hilbert space. Therefore, Equation (8) is termed as the *weak* formulation, which is the foundation for the well-known and widely used FEM.

## 2.2. Finite element settings

In practice, it is generally very difficult to solve the governing equations in either strong or weak forms in analytical means for the *exact* solution. We then often resort to numerical methods to obtain *approximate* solutions in discrete forms. The most popular method is the traditional FEM based on the weak formulation where the Galerkin projection is chosen to obtain an approximate solution  $\tilde{u}$  from a proper  $H^1$  space of lower and finite dimension. The FEM formulation can be conveniently done as long as we can create a proper discrete (hence finite)  $H^1$  space based on a mesh of elements. It is well known that such a FEM solution is the best (in energy norm) possible solution in the discrete finite element space  $\mathbb{H}_{h,0}^1(\Omega) \subset \mathbb{H}_0^1(\Omega)$  (see, e.g. [11]) that  $\tilde{u} \rightarrow u$  when  $\mathbb{H}_{h,0}^1(\Omega) \rightarrow \mathbb{H}_0^1(\Omega)$ , meaning that the approximate FEM solution will approach to the exact solution when the size of the element approaches to zero and the dimension of the FEM model is  $N_n \rightarrow \infty$ .

The finite element solution  $\tilde{u}$  as an approximation to the solution of the problem defined in Section 2 satisfies the following *weak* statement:

$$a(\tilde{u}, v) = f(v), \quad v \in (\mathbb{H}_{h,0}^1)^d \quad (9)$$

where displacement field  $\tilde{u} \in \mathbb{H}_{h,0}^1$  is expressed in terms of the following interpretation:

$$\tilde{u}(\mathbf{x}) = \sum_{i \in S_e} \varphi_i(\mathbf{x}) \tilde{d}_i \quad (10)$$

where  $\mathbf{x} = \{x_1, \dots, x_d\}^T$ ,  $S_e$  is the set of the nodes in the element that hosts  $\mathbf{x}$ ,  $\tilde{d}_i$  is a nodal displacement of FEM, and  $\varphi_i \in \mathbb{H}_{h,0}^1 \subset \mathbb{H}_0^1$  is a nodal basis functions that are the Kronecker delta:  $\varphi_i(\mathbf{x}_j) = \delta_{ij}$  at node  $i$ , and evaluated at coordinate  $\mathbf{x}_j$ .

We then substitute Equation (10) into Equation (9), and set  $\varphi_i$ ,  $i = 1, \dots, N_n$ , as the test function  $v$ , we have the following discrete set of  $N_n$  equations:

$$\sum_{j=1}^{N_n} a(\varphi_j, \varphi_i) \tilde{d}_j = f(\varphi_i), \quad i = 1, \dots, N_n \quad (11)$$

which can be written in the matrix form of

$$\tilde{\mathbf{K}} \tilde{\mathbf{d}} = \tilde{\mathbf{f}} \quad (12)$$

where  $\tilde{\mathbf{K}}$  is the FEM stiffness matrix with entries of  $\tilde{K}_{ij} = a(\varphi_j, \varphi_i)$ ,  $1 \leq i, j \leq N_n$ ,  $\tilde{\mathbf{d}}$  is the vector of nodal displacements  $\tilde{d}_i$ , and  $\tilde{\mathbf{f}}$  is the vector with entries of  $\tilde{f}_i = f(\varphi_i)$ .

### Remark 2.3 (Full compatibility)

A fully compatible FEM model satisfies three conditions: (1) the strain–displacement relation; (2) the essential (displacement) boundary conditions and (3) the shape functions  $\varphi_i$  are

compatible. To ensure the shape functions being *compatible* in a FEM setting, we practice mainly two tricks: (a) using only nodes of the element to create  $\varphi_i$  in the natural coordinate system and (b) use proper mapping for the element to ensure the continuity of  $\varphi_i$  on the interfaces of the elements.

*Remark 2.4 (Lower bound property)*

The strain energy computed using the fully compatible FEM solution  $\tilde{u} \in (\mathbb{H}_{h,0}^1)^d \subset (\mathbb{H}_0^1)^d$  is a lower bound of the exact strain energy computed using the exact solution  $u$ :

$$a(\tilde{u}, \tilde{u}) \leq a(u, u) \tag{13}$$

This property of FEM provides a good global measure of the lower bound of the FEM solution with respect to the exact solution.

Note that the weak formulation is also applied in meshfree settings [12].

### 3. BILINEAR FORMS IN G SPACES

#### 3.1. Definition

In this work, we focus on bilinear forms defined in  $\mathbb{G}_h^1(\Omega)$  spaces [1, 13] for mechanics problems for solids of stable materials. The bilinear form in  $\mathbb{G}_h^1$  spaces is also called the *smoothed* bilinear form because of the use of the generalized smoothed gradients [10].

Consider a solid mechanics problem governed by strong form PDEs given in Section 2. The problem domain  $\Omega$  is discretized with a background cells or elements, over which stationary smoothing domains are created following the rules detailed in Section 3.2. We require also that at least the minimum number of independent smoothing domains is used (see Section 3.8.5 in [1]). The bilinear form  $\bar{a}_D(w, v)$  is then defined as

$$\bar{a}_D(w, v) = \sum_{k=1}^{N_s} A_k^s \left( \underbrace{\frac{1}{A_k^s} \int_{\Gamma_k^s} w_i n_j \, ds}_{\bar{g}_{ij}(w)} \right) C_{ijkl} \left( \underbrace{\frac{1}{A_k^s} \int_{\Gamma_k^s} v_k n_l \, ds}_{\bar{g}_{kl}(v)} \right) = \sum_{k=1}^{N_s} A_k^s \underbrace{\bar{g}_{ij}(w) C_{ijkl} \bar{g}_{kl}(v)}_{\bar{a}_{D,k}(w,v)} \tag{14}$$

where  $w, v \in (\mathbb{G}_h^1)^d$ . Note that the summation is made possible by the particular way of creating the smoothing domains that ensures the continuity of the functions on  $\Gamma_k^s$ . In terms of the (generalized) *smoothed* strain,  $\bar{a}_D(w, v)$  may be written in the matrix form of (see, Section 2)

$$\bar{a}_D(w, v) = \sum_{k=1}^{N_s} A_k^s \bar{\boldsymbol{\epsilon}}_k^T(w) \mathbf{C} \bar{\boldsymbol{\epsilon}}_k(v) \tag{15}$$

where  $\bar{\epsilon}_k$  is the vector of the *smoothed* strains in the smoothed domain  $\Omega_k^s$  for given  $\mathbf{u} = \{w_1 \ w_2\}^T$  (for 2D case) with  $w \in (\mathbb{G}_h^1)^2$ , and is given by

$$\begin{aligned} \bar{\epsilon}_k(\mathbf{u}) &= \frac{1}{A_k^s} \int_{\Gamma_k^s} \mathbf{L}_n \mathbf{u}(\mathbf{x}) \, ds = \{\bar{\epsilon}_{11} \ \bar{\epsilon}_{22} \ 2\bar{\epsilon}_{12}\}_k^T \\ &= \left\{ \begin{array}{cc} \frac{\partial w_1}{\partial x_1} & \frac{\partial w_2}{\partial x_2} \\ \frac{\partial w_1}{\partial x_2} & \frac{\partial w_2}{\partial x_1} \end{array} \left( \underbrace{\frac{\partial w_1}{\partial x_2}}_{\bar{g}_{12}} + \underbrace{\frac{\partial w_2}{\partial x_1}}_{\bar{g}_{21}} \right) \right\}_k^T = \{\bar{g}_{11} \ \bar{g}_{22} \ (\bar{g}_{12} + \bar{g}_{21})\}_k^T \end{aligned} \tag{16}$$

3.2. Fourth inequality

The  $L^2$  norm of the strain vector  $\|\bar{\epsilon}\|_{L^2}^2$  can be written as

$$\|\bar{\epsilon}\|_{L^2}^2 = \sum_{k=1}^{N_s} A_k^s (\bar{\epsilon}_{11}^2 + \bar{\epsilon}_{22}^2 + 4\bar{\epsilon}_{12}^2) = \sum_{k=1}^{N_s} A_k^s (\bar{g}_{11}^2(w_1) + \bar{g}_{22}^2(w_2) + (\bar{g}_{12}(w_1) + \bar{g}_{21}(w_2))^2) \tag{17}$$

It is now clear that  $L^2$  norm of the strain vector is the same as the  $\mathbb{G}^1$  semi-norm (see, Equation (35) in [1]):

$$|w|_{\mathbb{G}^1(\Omega)} = \|\bar{\epsilon}\|_{L^2} \quad \forall w \in (\mathbb{G}_{h,0}^1)^2 \tag{18}$$

which will be useful in proving important properties in the following sections.

Combining Equation (72) in [1] and Equation (18), we obtain the 4th inequality:

$$c_G \|w\|_{\mathbb{G}^1(\Omega)} \leq \|\bar{\epsilon}\|_{L^2} \quad \forall w \in (\mathbb{G}_{h,0}^1)^2 \tag{19}$$

which is equivalent to the 2nd Korn’s inequality in an  $H^1$  space. Combining Equation (74) in [1] and Equation (18), we have the following chain inequality:

$$c_G \|w\|_{\mathbb{G}^1(\Omega)} \leq \|\bar{\epsilon}\|_{L^2} \leq \|w\|_{\mathbb{G}^1(\Omega)} \quad \forall w \in (\mathbb{G}_{h,0}^1)^2 \tag{20}$$

3.3. Properties of the smoothed bilinear form

Remark 3.1

By simple observation, it is clear that the smoothed bilinear form has basic properties of symmetry

$$\bar{a}_D(w, v) = \bar{a}_D(v, w) \quad \forall w, v \in (\mathbb{G}_{h,0}^1)^2 \tag{21}$$

for the symmetry property of the elastic material constants, and semi-positive definite

$$\bar{a}_D(w, w) \geq 0 \quad \forall w \in (\mathbb{G}_{h,0}^1)^2 \tag{22}$$

for the positivity of the materials constants.

Remark 3.2 (Convergence property for  $H^1$  space)

For  $w, v \in (\mathbb{H}^1)^d$ , when  $N_s \rightarrow \infty$  and all  $\Omega_k^s \rightarrow 0$ ,  $\bar{W}$  becomes Delta functions and the integral representation will be exact. At such a limit  $\bar{a}_D(w, v) \rightarrow a(w, v)$ . Therefore, based on the known

property of  $a(w, v)$  (see, Equation (5)), we should have the *ellipticity* property: meaning that there exists a nonzero positive constant  $c$  such that

$$\lim_{\substack{N_s \rightarrow \infty \\ \text{all } \Omega_k^s \rightarrow 0}} \bar{a}_D(w, w) \geq c \|w\|_{H^1(\Omega)}^2 \quad \forall w \in (\mathbb{H}_{h,0}^1)^d \tag{23}$$

The ellipticity ensures the existence and uniqueness of the solution of our W<sup>2</sup> formulation when the smoothing domain is refined (kept unchanged). When the  $\mathbb{H}^1$  space is enriched (element/cell mesh is refined, together the smoothing domains), the solution approaches to the exact solution. However, our goal is to have the smoothed bilinear form working for W<sup>2</sup> formulation of finite discretization of domains and functions in G<sup>1</sup> spaces, which requires the 5th inequality.

3.3.1. Ellipticity with respect to semi-norm.

Theorem 3.1

Ellipticity with respect to semi-norm: For solids of stable materials, there exists a nonzero positive constant  $c_{aw}^s$  such that

$$\bar{a}_D(w, w) \geq c_{aw}^s |w|_{G^1(\Omega)}^2 \quad \forall w \in (\mathbb{G}_{h,0}^1)^d \tag{24}$$

Proof

The proof starts from the definition Equation (15). For  $w \in (\mathbb{G}_{h,0}^1)^d$ , we have

$$\bar{a}_D(w, w) = \sum_{k=1}^{N_s} A_k^s \bar{\mathbf{e}}_k^T(w) \mathbf{C} \bar{\mathbf{e}}_k(w) = \sum_{k=1}^{N_s} A_k^s \bar{\mathbf{e}}_k^T(w) \underbrace{\mathbf{U}^T \mathbf{\Lambda} \mathbf{U}}_{\mathbf{C}} \bar{\mathbf{e}}_k(w) \tag{25}$$

used the fact that the material is stable, and hence the matrix of the elastic constants  $\mathbf{C}$  is SPD and can *always* be decomposed into unitary matrix  $\mathbf{U}$  of eigenvectors and diagonal matrix  $\mathbf{\Lambda}$  of all the positive eigenvalues. We further have

$$\begin{aligned} \bar{a}_D(w, w) &= \sum_{k=1}^{N_s} A_k^s \bar{\mathbf{e}}_k^T(w) \underbrace{\mathbf{U}^T \mathbf{\Lambda} \mathbf{U}}_{\mathbf{C}} \bar{\mathbf{e}}_k(w) = \sum_{s=1}^{N_s} A_k^s [\mathbf{U} \bar{\mathbf{e}}_k(w)]^T \mathbf{\Lambda} [\mathbf{U} \bar{\mathbf{e}}_k(w)] \\ &\geq \lambda_{\min} \underbrace{\sum_{s=1}^{N_s} A_k^s [\mathbf{U} \bar{\mathbf{e}}_k(w)]^T [\mathbf{U} \bar{\mathbf{e}}_k(w)]}_{\leq \|\mathbf{U} \bar{\mathbf{e}}(w)\|_{L^2}^2 = \|\bar{\mathbf{e}}(w)\|_{L^2}^2} \geq \lambda_{\min} \|\bar{\mathbf{e}}(w)\|_{L^2}^2 = \underbrace{\lambda_{\min}}_{c_{aw}^s} |w|_{\mathbb{G}^1(\Omega)}^2 \end{aligned} \tag{26}$$

where  $\lambda_{\min}$  is the smallest eigenvalue of  $\mathbf{C}$ . In the 2nd line of the above equation, we used the facts (1)  $L^2$  norm definition by inner product; (2) a unitary matrix preserves  $L^2$  norms; and (3) the  $L^2$  norm of the strain vector is the same as the semi-norm (see, Equation (18)). Finally, we have the 5th inequality Equation (24), by letting  $c_{aw}^s = \lambda_{\min}$ . □

3.3.2. *Fifth inequality.*

*Theorem 3.2 (Ellipticity (coercivity))*

For solids of stable materials, there exists a nonzero positive constant  $c_{aw}^f$  such that

$$\bar{a}_D(w, w) \geq c_{aw}^f \|w\|_{\mathbb{G}^1(\Omega)}^2 \quad \forall w \in (\mathbb{G}_{h,0}^1)^d \tag{27}$$

which implies the *ellipticity* or *coercivity* of bilinear forms in a  $\mathbb{G}^1$  space.

*Proof*

From Equation (72) in [1] and Equation (24), we immediately have

$$\bar{a}_D(w, w) \geq c_{aw}^s |w|_{\mathbb{G}^1}^2 \geq \underbrace{c_{aw}^s c_G}_{c_{aw}^f} \|w\|_{\mathbb{G}^1}^2 \tag{28}$$

which is the 5th inequality Equation (27). □

Theorem 3.2 is important because it ensures, the existence (and hence the uniqueness) and consequently the stability of the solution of a  $W^2$  formulation.

3.3.3. *Sixth inequality.*

*Theorem 3.3 (Bounded property (continuity))*

For solids of stable materials, there exists a nonzero positive constant  $c_{awv}^f$  such that

$$\bar{a}_D(w, v) \leq c_{awv}^f |w|_{\mathbb{G}^1(\Omega)} |v|_{\mathbb{G}^1(\Omega)} \quad \forall w \in (\mathbb{G}_{h,0}^1)^d \quad \forall v \in (\mathbb{G}_{h,0}^1)^d \tag{29}$$

and

$$\bar{a}_D(w, v) \leq c_{awv}^f \|w\|_{\mathbb{G}^1(\Omega)} \|v\|_{\mathbb{G}^1(\Omega)} \quad \forall w \in (\mathbb{G}_{h,0}^1)^d \quad \forall v \in (\mathbb{G}_{h,0}^1)^d \tag{30}$$

*Proof*

We start again from the definition Equation (15). For  $w, v \in (\mathbb{G}_{h,0}^1)^d$ , we have

$$\bar{a}_D(w, v) = \sum_{k=1}^{N_s} A_k^s \bar{\mathbf{e}}_k^T(w) \mathbf{C} \bar{\mathbf{e}}_k(v) = \sum_{k=1}^{N_s} A_k^s \bar{\mathbf{e}}_k^T(w) \underbrace{\mathbf{U}^T \mathbf{\Lambda} \mathbf{U}}_{\mathbf{C}} \bar{\mathbf{e}}_k(v) \tag{31}$$

where the positivity of the material constants is again used to decompose  $\mathbf{C}$ . Equation (3.3.4) becomes

$$\begin{aligned} \bar{a}_D(w, v) &= \sum_{k=1}^{N_s} A_k^s \bar{\mathbf{e}}_k^T(w) \underbrace{\mathbf{U}^T \mathbf{\Lambda} \mathbf{U}}_{\mathbf{C}} \bar{\mathbf{e}}_k(v) = \sum_{k=1}^{N_s} A_k^s [\mathbf{U} \bar{\mathbf{e}}_k(w)]^T \mathbf{\Lambda} [\mathbf{U} \bar{\mathbf{e}}_k(v)] \\ &\leq \lambda_{\max} \underbrace{\sum_{k=1}^{N_s} A_k^s [\mathbf{U} \bar{\mathbf{e}}_k(w)]^T [\mathbf{U} \bar{\mathbf{e}}_k(v)]}_{\leq \| \mathbf{U} \bar{\mathbf{e}}(w) \|_{L^2} \| \mathbf{U} \bar{\mathbf{e}}(v) \|_{L^2} = \| \bar{\mathbf{e}}(w) \|_{L^2} \| \bar{\mathbf{e}}(v) \|_{L^2}} \leq \lambda_{\max} \| \bar{\mathbf{e}}(w) \|_{L^2} \| \bar{\mathbf{e}}(v) \|_{L^2} \end{aligned} \tag{32}$$

$$\begin{aligned}
 &= \underbrace{\lambda_{\max}^f}_{c_{awv}^f} |w|_{\mathbb{G}^1(\Omega)} |v|_{\mathbb{G}^1(\Omega)} = c_{awv}^f |w|_{\mathbb{G}^1(\Omega)} |v|_{\mathbb{G}^1(\Omega)} \\
 &\leq c_{awv}^f \|w\|_{\mathbb{G}^1(\Omega)} \|v\|_{\mathbb{G}^1(\Omega)} = c_{awv}^f \|w\|_{\mathbb{G}^1(\Omega)} \|v\|_{\mathbb{G}^1(\Omega)}
 \end{aligned}$$

where  $\lambda_{\max}$  is the largest eigenvalue of  $\mathbf{C}$ . In the 2nd line of the above equation, we used the facts (1) the Cauchy–Schwarz inequality for inner product induced  $L^2$  norm, (2) a unitary matrix preserves  $L^2$  norms, and (3) the  $L^2$  norm of the strain vector equals the semi-norm (see, Equation (18)). In the 3rd line, we used Equation (49) in [1]: a semi-norm is no larger than the full norm. Finally, we have 6th inequality Equation (30), by letting  $c_{awv}^f = \lambda_{\max}$ .  $\square$

Theorem 3.3 is important because it ensures that our bilinear form is continuous. Together with the stability, we will have the convergence of the solution of a  $W^2$  formulation.

3.3.4. *Softened model.*

*Theorem 3.4*

*Softened model:* For stable materials and any  $w \in (\mathbb{H}_h^1)^d$  the smoothed bilinear form is smaller than the bilinear form:

$$\bar{a}_D(w, w) \leq a(w, w) \quad \forall w \in (\mathbb{H}_h^1)^d \tag{33}$$

The proof of the inequality Equation (33) is quite similar to the 4th inequality Equation (75) in [1], and a more general inequality than Equation (33) can be found in [10].

Theorem 3.4 implies that a model established based on the smoothed bilinear will be ‘softer’ than that of bilinear form which was discovered in [14].

3.3.5. *Monotonic convergence.*

*Theorem 3.5*

*Monotonic convergence property:* In a given division  $D_1$  of domain  $\Omega$  into a set of smoothing domains  $\boxed{\Omega} = \bigcup_{k=1}^{N_s} \boxed{\Omega}_k^s$  where the box stands for enclosed domain, if a new division  $D_2$  is created by sub-dividing a smoothing domain in  $D_1$  into  $n_{sd}$  sub-smoothing-domains:  $\boxed{\Omega}_k^s = \bigcup_{j=1}^{n_{sd}} \boxed{\Omega}_{k,j}^s$ , then the following inequality stands:

$$\bar{a}_{D_1}(w, w) \leq \bar{a}_{D_2}(w, w) \tag{34}$$

which was found in [14]. Theorem 3.5 implies that the ‘softening’ effect provided by the  $W^2$  formulation will be monotonically reduced with the increase of the number of smoothing domain in a nested manner. One now has the freedom to reduce or increase the stiffness or softness of the model as desired.

Finally, we present the following Cauchy–Schwarz inequality for our smoothed bilinear form, as it can be very useful in the derivation of important properties of our  $W^2$  formulations.

*Theorem 3.6*

Cauchy–Schwarz inequality for our smoothed bilinear form: For solids of stable materials, we shall have

$$|\bar{a}_D(w, v)| \leq \sqrt{\bar{a}_D(w, w)} \sqrt{\bar{a}_D(v, v)} \quad \forall w, v \in (\mathbb{G}_h^1)^d \tag{35}$$

*Proof*

Because the material is stable, we shall have  $\mathbf{C} = \mathbf{U}^T \mathbf{\Lambda} \mathbf{U}$ , where diagonal matrix  $\mathbf{\Lambda}$  are the positive eigenvalues.

$$\begin{aligned} \bar{a}_D(w, v) &= \sum_{k=1}^{N_s} A_k^s \bar{\mathbf{\epsilon}}_k^T(w) \underbrace{\mathbf{U}^T \mathbf{\Lambda} \mathbf{U}}_{\mathbf{C}} \bar{\mathbf{\epsilon}}_k(v) = \sum_{k=1}^{N_s} A_k^s \bar{\mathbf{\epsilon}}_k^T(w) \underbrace{(\mathbf{U}^T \sqrt{\mathbf{\Lambda}} \mathbf{U})(\mathbf{U}^T \sqrt{\mathbf{\Lambda}} \mathbf{U})}_{\mathbf{C}} \bar{\mathbf{\epsilon}}_k(v) \\ &= \sum_{k=1}^{N_s} A_k^s [\mathbf{U}^T \sqrt{\mathbf{\Lambda}} \mathbf{U} \bar{\mathbf{\epsilon}}_k(w)]^T [\mathbf{U}^T \sqrt{\mathbf{\Lambda}} \mathbf{U} \bar{\mathbf{\epsilon}}_k(v)] \\ &\leq \underbrace{\|\mathbf{U}^T \sqrt{\mathbf{\Lambda}} \mathbf{U} \bar{\mathbf{\epsilon}}_k(w)\|_{L^2}}_{\sqrt{\|\bar{\mathbf{\epsilon}}_k^T(w) \mathbf{C} \bar{\mathbf{\epsilon}}_k(w)\|_{L^2} = \sqrt{\bar{a}_D(w, w)}}} \underbrace{\|\mathbf{U}^T \sqrt{\mathbf{\Lambda}} \mathbf{U} \bar{\mathbf{\epsilon}}_k(v)\|_{L^2}}_{\sqrt{\|\bar{\mathbf{\epsilon}}_k^T(v) \mathbf{C} \bar{\mathbf{\epsilon}}_k(v)\|_{L^2} = \sqrt{\bar{a}_D(v, v)}}} = \sqrt{\bar{a}_D(w, w)} \sqrt{\bar{a}_D(v, v)} \end{aligned} \tag{36}$$

where  $\sqrt{\mathbf{\Lambda}}$  denotes a diagonal matrix with the square roots of all the eigenvalues of  $\mathbf{\Lambda}$ . □

### 4. WEAKENED WEAK ( $W^2$ ) FORMULATION

*4.1.  $W^2$  statement*

For solid mechanics problems given in the strong statements in Section 2, our  $W^2$  statement is given as follows. The weakened weak ( $W^2$ ) solution  $\bar{u} \in (\mathbb{G}_{h,0}^1)^d$  satisfies

$$\bar{a}_D(\bar{u}, v) = f(v) \quad \forall v \in (\mathbb{G}_{h,0}^1)^d \tag{37}$$

where  $\bar{a}_D$  is defined in Section 3.1. Note here that we make no changes to the linear functional (because it cannot and need not be further weakened), and the displacements are assumed in the same form as in Equation (6) in [1] with shape functions properly constructed in either the standard FEM or meshfree context. We now state that.

*Remark 4.1*

If the solution is sought from a proper H space, the  $W^2$  statement Equation (37) is variationally consistent in the standard weak formulation and hence the solution will be unique and will converge to the exact solution of the strong statement.

The proof for Remark 4.1 can be found in [14], and hence will not be repeated here. However, our goal is to have the  $W^2$  statement work for functions in  $G^1$  spaces, which is ensured by the following theorem.

*Theorem 4.1 (Unique solution)*

For solids of stable materials, the  $W^2$  statement Equation (37) has a unique solution.

*Proof*

To prove Theorem 4.1, we need to show two key ingredients in the  $W^2$  formulation: (1) the bilinear form is of *ellipticity* to ensure the existence of the solution, and (2) the bilinear form is continuous to ensure that the solution is bounded. Note the ellipticity has already been given by Theorem 3.2 or Equation (27), and the boundedness is given by Theorem 3.3 or Equation (30). Based on the Lax–Milgram theorem, Equations (27) and Equation (30) ensures a  $W^2$  formulation has a unique solution. This completes the proof of Theorem 4.1.  $\square$

We state that the unique solution the  $W^2$  statement will converge to the exact solution of the original strong form. A proof for this statement can be found in that of Theorem 5.7 (or Theorem 5.5b) presented in [15].

*Remark 4.2*

Note that the  $W^2$  statement Equation (37) is in fact a generalized Galerkin formulation as the trial and test functions are all from the same proper G space, but in a much more general setting for solution spaces. It was termed as generalized smoothed Galerkin formulation [10], when the G space theory was not well established with properly proven theories. With the G space theory established in this paper, it is clear now that we have a very general framework for establishing a wide class of computational methods. Clearly, we do not have to confirm ourselves within the Galerkin formulation. It opens to all sorts of possibilities beyond the Galerkin formulation, such as the Petrov–Galerkin and least-square formulations. Even within the Galerkin formulation, we now have plenty freedoms to create the smoothing domains, and to create shape functions using FEM settings and meshfree settings. Furthermore, even within the FEM setting, there are now many avenues to explore. Just for an example, we can now use different shapes of elements [8, 16, 17], mixed shapes of elements, and even mixed elements of different order, because the compatibility worry is now off the way in our  $W^2$  formulation. We will show some of the interesting examples in Section 6.

*4.2.  $W^2$  formulation procedure*

A  $W^2$  model can be established based on any setting of a FEM model [18]: we simply use exactly the same mesh of the FEM, but create an additional overlay mesh of smoothing domains. These domains can be based on elements or nodes or edges of the elements. Such models have already been created and known as the SFEM [8, 16, 17], NS-FEM [5, 6], and ES-FEM [6]. Note that the FEM shape functions used in a  $W^2$  model do not have to be continuous, which means that one can practically use elements of mixed orders. The only thing that one needs to make sure is that the interface lines of the smoothing domain do not share any finite part of these discontinuous lines in the FEM model with mixed order of elements.

A more general  $W^2$  formulation can be based on meshfree settings. In such cases, we often use a set of triangular background cells, although any other type of background cells can also be used. We prefer triangular cells because they can be created much more easily in an automatic fashion compared with other types of cells. Upon the background cells, we create a set of non-gap and non-overlap smoothing domains. In the meshfree settings, the shape functions are often discontinuous, and hence we need to make sure that the boundaries of these smoothing domains do not share any finite portion of the lines where the nodal shape functions are discontinuous. Typical  $W^2$  models are the NS-PIM [2, 3], NS-RPIM [9], ES-PIM [19], ES-RPIM [19], ES-PIM [20], and CS-PIM [20].

Once the  $W^2$  model is created, the formulation procedure is largely the same as that in a standard FEM model, described in Section 2.2. In the following we will demonstrate a number of existing  $W^2$  models, and some of the newly created ones.

## 5. POSSIBLE $W^2$ MODELS

We now introduce a number of  $W^2$  models that can largely be divided into two groups: FEM settings and meshfree settings. For models of FEM settings, the displacement functions are continuous, compatible and hence in an  $H^1$  space, but we use  $W^2$  formulation; while in meshfree settings, the displacement functions are, in general, discontinuous, incompatible, and hence in a  $G^1$  space. The following discussion will be brief on models of FEM settings, and in more detail on meshfree settings, in particular the PIM settings.

### 5.1. Smoothed finite element method (SFEM)

One typical  $W^2$  model is the so-called smoothed finite element method (SFEM) [8, 16, 17]. In the SFEM, the physical domain  $\Omega$  is first meshed with  $N_e$  elements of say, quadrilaterals as we do in the FEM procedure, and an element is further divided to form a number of smoothing domains/cells, as shown in Figure 1, which gives a total of  $N_s$  smoothing domains, and  $\bar{\Omega} = \bigcup_{k=1}^{N_s} \bar{\Omega}_k$ . In this case we shall have  $N_e \leq N_s$ .

The SFEM uses the FEM shape functions created based on elements and it requires little change to the FEM codes. Note that in the SFEM formulation,  $n$ -sided polygonal elements can be used [17]. In such cases, the shape functions are constructed using simple point interpolation

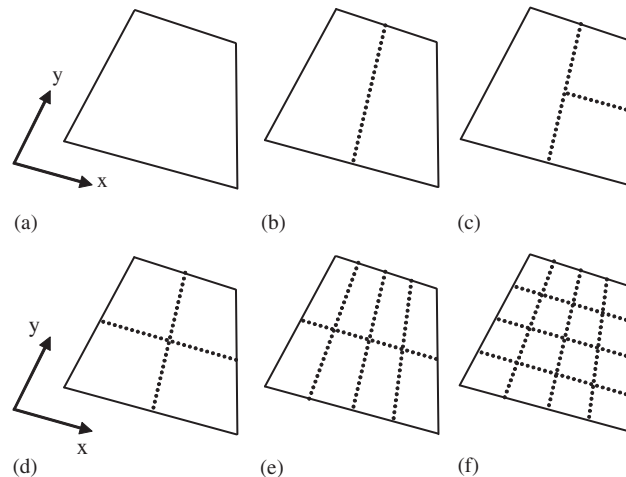


Figure 1. SFEM model [16]: Division of an quadrilateral element in a FEM mesh into smoothing domains/cells (SC): (a) Only one smoothing cell is used for the element (SC=1); (b) two smoothing cells are used for the element (SC=2), and so on. The smoothed strains each of these cell areas of used individually to compute the stiffness matrix; (c) SC=3; (d) SC=4; (e) SC=8; and (f) SC=16.

procedures and no mapping is required. When linear triangular elements are used, the smoothing operation to the elements has no effect at all, regardless of how many smoothing cells are used in an element, and hence the SFEM produces the same solution as the FEM. Many other good properties of SFEM have been found such as resilience to the element mesh distortion accurate in stress solution, etc. In general, when  $N_s \rightarrow \infty$ , the SFEM become the FEM, if the same set of shape functions in a proper H space can be used. Readers are referred to [8, 16, 17] for more details.

### 5.2. Node-based smoothed finite element method (NS-FEM)

A node-based SFEM or NS-FEM [5] has been proposed recently, and applied to  $n$ -sided polygonal elements. In the NS-FEM, the smoothing domains are node-based, as shown in Figure 2. The problem domain  $\Omega$  is meshed with  $N_e$  elements of  $n$ -sides with a total of  $N_n$  nodes as we do in the FEM procedure. Then  $N_s$  smoothing domains are formed with each  $\Omega_k^s$  which contains a node and covers the portions of the elements sharing this node. Therefore, in this case  $N_s = N_n$ , satisfying the minimum number of smoothing domains. It is found that the NS-FEM can produce the upper bound solutions [5]. When linear triangular elements are used, the NS-FEM is the same as the NS-PIM using linear interpolations [2].

### 5.3. Edge-based smoothed finite element method (ES-FEM)

An edge-based SFEM or ES-FEM has been proposed recently for general  $n$ -sided elements [6]. In the ES-FEM, the smoothed Galerkin weakform is also used and the procedure is almost the same as the NS-FEM, except that the smoothing domains are created based on the edges of the elements, as shown in Figure 3. The ES-FEM was devised to remove the spurious modes observed in NS-FEM by simply changing the way of constructing the smoothing domains. This simple change has made the mode with a ‘close-to-exact’ stiffness for accurate solution, and successfully

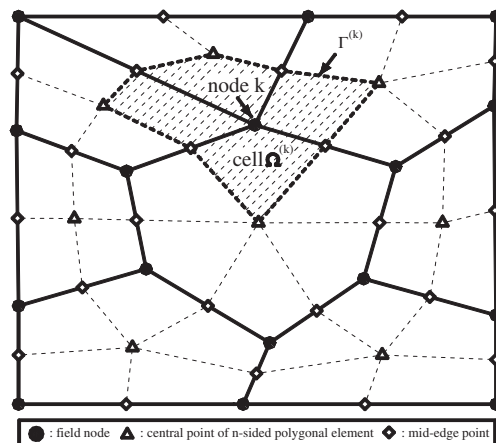


Figure 2. NS-FEM model [5]:  $n$ -sided polygonal elements (bounded by solid edges) and the non-overlapping stationary smoothing cells/domains (shaded areas) associated with node  $k$ . The smoothed strains of each of these smoothing cells are used individually to compute the stiffness matrix.

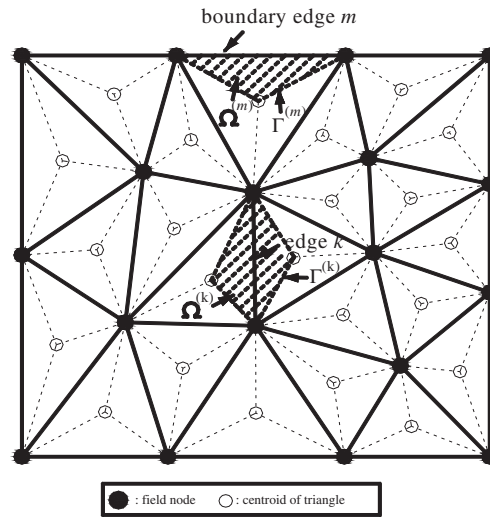


Figure 3. ES-FEM model [6]: Triangular elements (bounded by solid lines) and the smoothing domain  $\Omega$  (shaded areas) created by sequentially connecting the centroids of the surrounding triangles of an edge with the nodes on the edge. The smoothed strains of each of these smoothing domains are used individually to compute the stiffness matrix.

solved the spurious modes when solving dynamic problems [6]. When linear triangular elements are used, the ES-FEM is the same as the ES-PIM using linear interpolations. For 3D problems, the ES-FEM becomes FS-FEM [7], in which we use face-based smoothing domains [6].

#### 5.4. Cell-based smoothed point interpolation method (CS-PIM)

The CS-PIM [20] model is developed using cell-based smoothing domains, which is similar as in the SFEM [6]. The difference is that: (1) the CS-PIM prefers using triangular cells and (2) CS-PIM uses PIM or RPIM shape functions that can be discontinuous in the smoothing cells. When linear shape functions created using two nodes on a triangular cell edge are used, the CS-PIM is the same as the linear FEM using the same triangular mesh. Details on CS-PIM can be found in the recent paper [20].

#### 5.5. Node-based smoothed point interpolation method (NS-PIM)

The NS-PIM model was developed in 2005 [2], and is in fact the earliest  $W^2$  model developed using discontinuous shape function created using PIM or RPIM using local support domains that are generally overlapping [15]. The NS-PIM generally uses a triangular mesh for guiding the node selection for the interpolation and for the smoothing domain construction, because a triangular mesh can be generated automatically for complicated problem domains. The problem domain  $\Omega$  is meshed with  $N_e$  elements of, say, triangles with a total of  $N_n$  nodes as we do in the FEM procedure. Based on these triangular elements, the domain is then divided into  $N_s$  node-based smoothing domains  $\square\Omega = \bigcup_{k=1}^{N_s} \square\Omega_k^s$ , and each  $\Omega_k^s$  contains a node and covers portions of elements sharing the node [1, 14, 21], as shown in Figure 3 in [1].

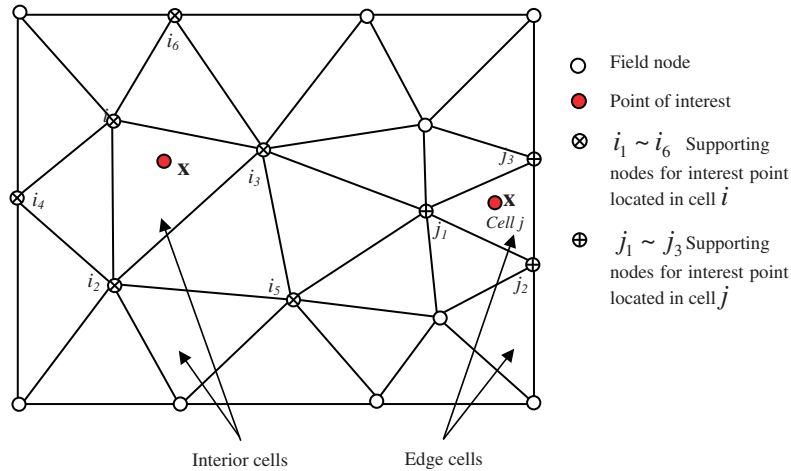


Figure 4. Supporting node selection in PIMs for shape function construction. For linear interpolations, three nodes of the triangular cell hosting  $x$  are selected. For quadratic interpolations, six nodes (three nodes of the triangular cell hosting  $x$ , and three nodes locate in the remote vertices for the three neighboring cells) are selected. In RPIM interpolations, all the nodes that are directly connected to the three nodes of the triangular cell hosting  $x$  are selected.

The selection of nodes for creating PIM and RPIM shape functions is illustrated in Figure 4. For linear interpolations, three nodes of the triangular cell hosting the point of interest  $x$  are selected. For quadratic interpolations, six nodes (three nodes of the triangular cell hosting  $x$ , and three nodes located in the remote vertices for the three neighboring cells) are selected. When the hosting cell is located on the boundary, we always use three nodes. In RPIM interpolations, all the nodes that are directly connected to the three nodes of the triangular cell hosting  $x$  are selected. The procedure for computing these shape functions is given in very detail in [22]. The PIM or RPIM shape functions constructed are not compatible except the linear interpolation case. Our W<sup>2</sup> formulation works well for these incompatible functions, as will be shown in the example problems.

Note that when linear shape functions are used, the NS-PIM and NS-FEM give the same results for the same triangular mesh used [2].

### 5.6. Edge-based smoothed point interpolation method (ES-PIM)

The ES-PIM model is developed in this work using edge-based smoothing domains, which is the same as in the ES-FEM [6]. The difference is that ES-PIM using PIM or RPIM shape function can be discontinuous. When linear shape functions are used, the ES-PIM and ES-FEM give the same results for the same triangular mesh used [6].

## 6. NUMERICAL EXAMPLES

We now present four numerical examples to examine the theories presented in this work. Our numerical study will focus on NS- and ES-PIM models. For NS- and ES-FEM models, readers

are referred to [5, 6, 8, 16, 17]. In the following study, the numerical errors are quantified using the following formulations. For displacements:

$$e_d = \sqrt{\frac{\sum_{i=1}^n (u_i^{\text{exact}} - u_i^{\text{numerical}})^2}{\sum_{i=1}^n (u_i^{\text{exact}})^2}} \quad (38)$$

which quantifies the error in the primary variable of our problem and is important to many analysts. The error in strain energy is evaluated numerically using

$$e_e = \frac{1}{A} \sqrt{\frac{1}{2} \sum_{i=1}^{N_Q} A_i (\boldsymbol{\epsilon}_i^{\text{exact}} - \boldsymbol{\epsilon}_i^{\text{numerical}})^T (\boldsymbol{\epsilon}_i^{\text{exact}} - \boldsymbol{\epsilon}_i^{\text{numerical}})} \quad (39)$$

where  $A$  is the area of the problem domain,  $A_i$  is the area of the  $i$ th integration cell (which is the smoothing domain for present methods, and element for FEM), and  $N_Q$  is the number of integration cells and is given by

$$N_Q = \begin{cases} N_s & \text{(for present methods)} \\ N_e & \text{(for FEM)} \end{cases} \quad (40)$$

in which  $N_s$  is the number of smoothing domains and  $N_e$  is the number of elements. All the strains are evaluated at the center of the integration cell. The error in strain energy of our problem is important to confirm our theory.

### 6.1. Standard patch tests

The theories presented in this work are new and need to be confirmed numerically. The first numerical test is the standard patch test for any weak form method to test on the convergence: a method passing the standard patch test is capable of producing solutions approaching the exact solution of any order when the mesh is refined. We consider a 2D patch of unit square with irregularly distributed 109 nodes generated in a random fashion with an irregular factor of 0.2, as shown in Figure 5. The randomness is injected for removal of obvious ‘coincidence’ in the node distribution in the patch. Linearly distributed displacements are specified on the four edges of the patch using the following equations:

$$\begin{aligned} u_1(x, y) &= 0.6x \\ u_2(x, y) &= 0.6y \end{aligned} \quad (41)$$

The exact solution for this patch should be a linear displacement field given by Equation (41) over the entire patch. A similar 3D patch of a cub is also designed with 166 irregularly distributed nodes. The results for both 2D and 3D patch tests are listed in Table I. It is clearly shown that all these schemes pass the patch tests to machine accuracy, including the ones using discontinuous functions in  $\mathbb{G}_h^1$  spaces. This ensures that all these methods are capable of reproducing linear field exactly and hence will converge to exact solutions of arbitrary order of continuity, because we have proven in theory the stability of the models. Note that we have also tested a number of other patches with different number of nodes and various arbitrary nodal arrangements. All of the

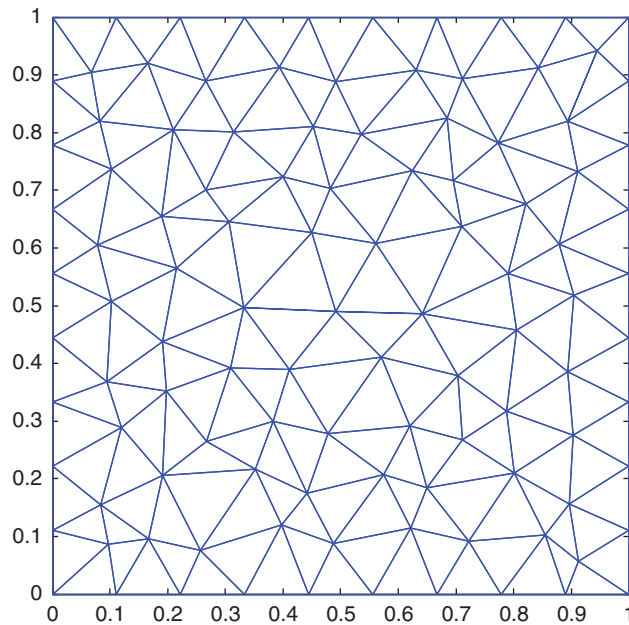


Figure 5. A 2D patch of unit square with irregularly distributed 109 nodes generated with a random factor of 0.2.

Table I. Errors in numerical results in displacement norm  $e_d$  for 2D and 3D patches.

Methods	2D	3D
NS-PIM (linear, compatible)	2.0852432E-15	1.2441043E-15
NS-PIM (quadratic, incompatible)	1.9425082E-14	Not conducted
ES-PIM (linear, compatible)	1.3586671E-15	4.6522876E-16
ES-PIM (quadratic, incompatible)	1.1453597E-14	Not conducted
NS-RPIM (local RBF, incompatible)	9.6473926E-16	7.6975097E-16
ES-RPIM (local RBF, incompatible)	1.5495214E-15	6.7286606E-14

patch tests are passed to the machine accuracy. This is because the assumed displacement field is linearly complete, and our model is proven stable. Note that for 3D problems, we have only developed high-order codes for NS-RPIM and ES-RPIM, but not for the NS-PIM and ES-PIM, because NS-RPIM and ES-RPIM are much more robust for nodes selection in 3D situations, and is clearly preferred for 3D problems.

### 6.2. Cantilever loaded at the end

A cantilever of length  $L$  and height  $D$  subjected to a parabolic traction at the free end as shown in Figure 6 is studied here using  $W^2$  models. The cantilever is assumed to have a unit thickness and under the plane stress condition. The analytical solution is available and can be found in a

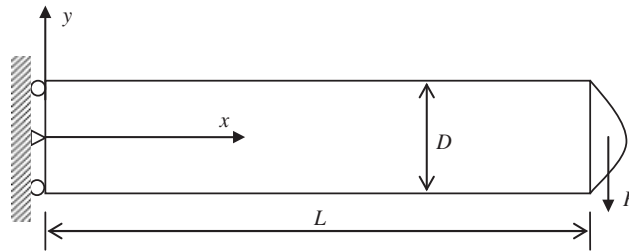


Figure 6. Cantilever loaded with a parabolically distributed load at the end.

textbook by Timoshenko and Goodier [23].

$$\begin{aligned}
 u_x &= -\frac{py}{6EI} \left[ (6L-3x)x + (2+\nu) \left( y^2 - \frac{D^2}{4} \right) \right] \\
 u_y &= \frac{p}{6EI} \left[ 3\nu y^2(L-x) + (4+5\nu) \frac{D^2 x}{4} + (3L-x)x^2 \right]
 \end{aligned} \quad (42)$$

where the moment of inertia  $I$  for a beam with rectangular cross-section and unit thickness is given by  $I = D^3/12$ .

The stresses corresponding to the displacements Equation (42) are

$$\sigma_{xx}(x, y) = \frac{-p(L-x)y}{I}, \quad \sigma_{yy}(x, y) = 0, \quad \tau_{xy}(x, y) = -\frac{p}{2I} \left( \frac{D^2}{4} - y^2 \right) \quad (43)$$

The related parameters are taken as  $E = 3.0 \times 10^7$  Pa,  $\nu = 0.3$ ,  $D = 10$  m,  $L = 50$  m, and  $P = -1000$  N. In the computations, the nodes on the left boundary are constrained using the exact displacements obtained from Equation (42) and the loading on the right boundary uses the distributed parabolic shear stresses in Equation (43). We use again irregularly distributed nodes generated in a random fashion with an irregular factor of 0.25, and the node distribution and triangular meshes are plotted in Figure 7. The randomness is injected for removal of any possible obvious ‘coincidence’ in the numerical models and this same set of meshes are used to examine all the methods to provide a common ground for comparisons.

Figure 8 plots the deflection of the cantilever along the neutral line ( $y=0$ ) obtained using different methods and the same irregular mesh with 801 nodes. In terms of displacement, all the methods give very good results and it is hard to distinguish them from this figure. Figure 9 plots the shear stress distribution along the cross-section of the cantilever at  $x=L/2$  obtained using different methods and the same mesh. The discrepancies are mainly observed on the surfaces of the beam. It seems that the PIMs perform better than the FEM. We, however, need more precise examinations to quantify the accuracy in these solutions.

Figure 10 plots the convergence of the solutions in displacement norm for the cantilever solved using different methods and the same set of irregular meshes. The solutions of all the methods converge and have about the same convergence rate. This confirms Theorem 4.1 and supports the discussions given in Section 4.2 in [1]. All the PIMs give more accurate solutions compared with the FEM, except the linear NS-PIM which is about the same as the FEM. The quadratic NS-PIM gives a better solution than the linear NS-PIM. Note that the quadratic PIM shape functions are

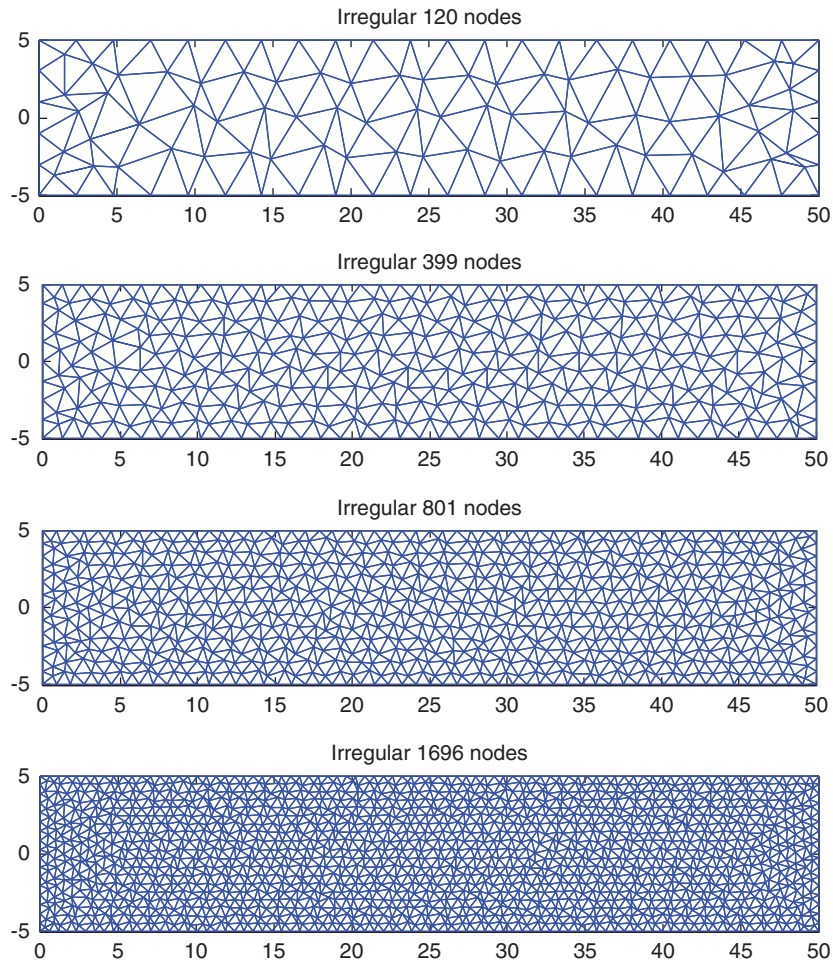


Figure 7. Irregularly distributed nodes generated using randomly with an irregular factor of 0.25 for the cantilever. These meshes will be used to examine all the methods.

created using the same mesh as in the linear PIM, which is different from a quadratic FEM model that has middle edge nodes and hence the nodal density would be about doubled compared with the linear FEM model. Although the order of approximation is increased in quadratic PIMs, the nodal spacing is not changed at all. Therefore, the accuracy improvement is not significant, as shown in Figure 10. In addition, the smoothing operations (with constant smoothing functions) used discount somewhat the higher-order approximation in the function. The ES-PIM family performs extremely well, and it is about 10 times more accurate than the FEM, especially the linear ES-PIM. This reflects the theoretical discussions given in Section 4.2 in [1]. In addition, we observe that the numerical rates of convergence in displacement norm of PIM models are roughly about the same as that of the FEM model with a theoretical value of 2.0. This again reflects the theoretical discussions on convergence rate in  $L^2$  norm given in Section 4.2 in [1]. We note that in linear FEM models,

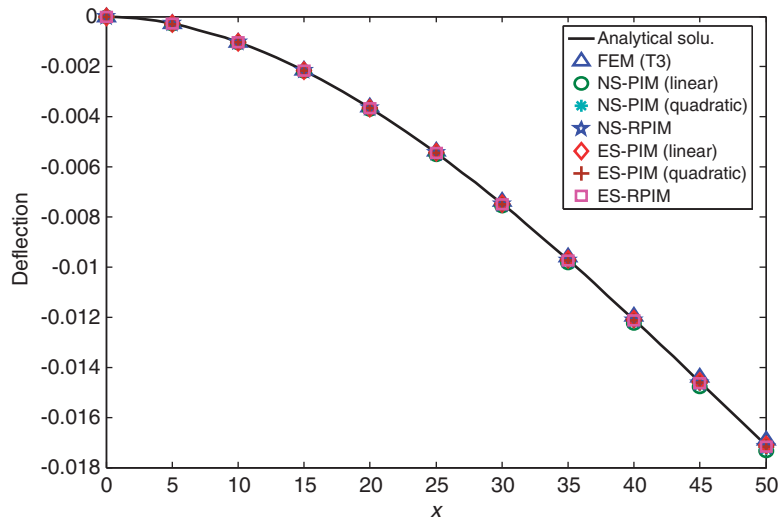


Figure 8. Deflection of the cantilever along the neutral line ( $y=0$ ) obtained different methods and the same irregular mesh with 801 nodes. In terms of displacement, all the methods give very good results and it is hard to distinguish them from this figure.

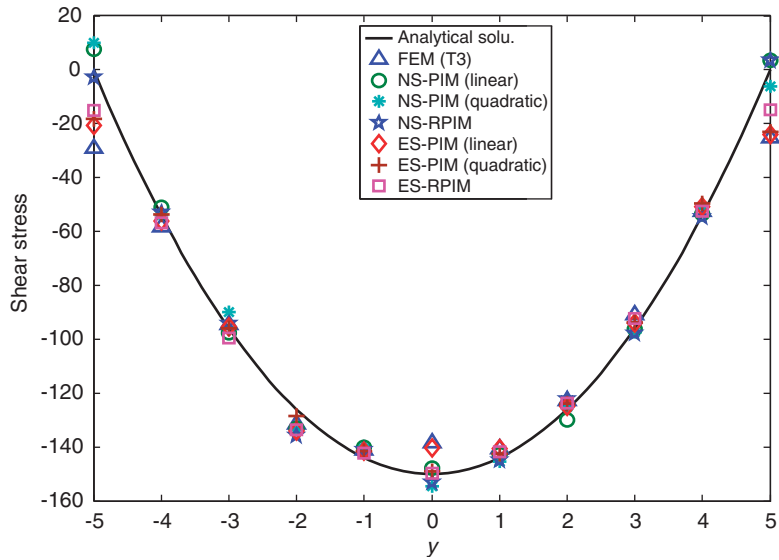


Figure 9. Shear stress distribution along the cross-section of the cantilever at  $x=L/2$  obtained different methods and the same irregular mesh with 801 nodes. The discrepancies are observed on the surfaces of the beam. It seems that the PIMs perform better than the FEM.

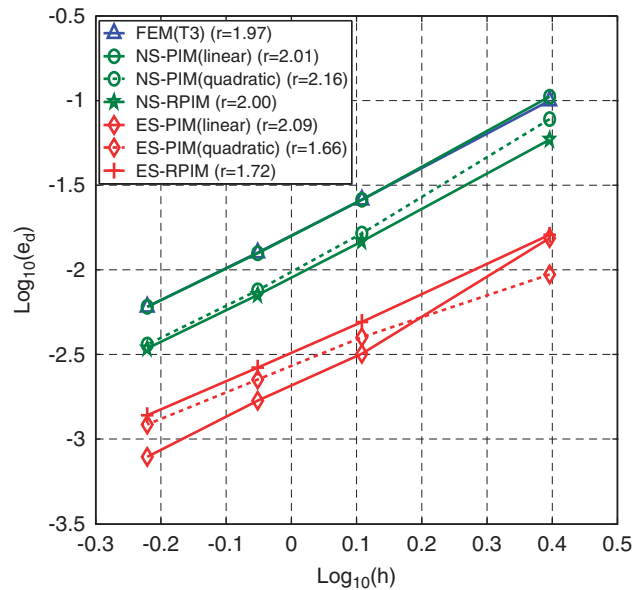


Figure 10. Convergence of the solutions in displacement norm for the cantilever solved using different methods and the same set of irregular triangular mesh. All the methods have about the same convergence rate, and all the PIMs give more accurate solution compared with the FEM, except the linear NS-PIM that is about the same as the FEM. The ES-PIM family performs extremely well, and its about 10 times more accurate than the FEM. The quadratic NS-PIMs gives better solution than the linear NS-PIM, but the quadratic ES-PIM is a little worse than the linear ES-PIM.

the convergence rate of the interpolation error in  $L^2$  norm is the same as the error in displacement norm defined in Equation (39). For our  $W^2$  formulation, we expect a similar relationship, but it is yet to be established theoretically.

Note that the quadratic ES-PIM is a little worse than the linear ES-PIM. This is because of the extremely high accuracy of the linear ES-PIM, in addition to the reasons mentioned earlier for the NS-PIM case. The RPIM performs roughly about the same as the quadratic PIMs. As radial basis functions are used in the shape function construction, the RPIM works particularly well for extremely irregularly distributed nodes, as reported in [5].

Figure 11 plots the convergence of the solutions in strain energy norm for the cantilever solved using different methods and the same set of irregular meshes. As the energy errors measured in  $H^1$  norm and  $G^1$  norm is a little different, the following comparison in energy norm may not be fair to the FEM, and hence is only indicative. All the PIM methods converge very well and have much higher accuracy compared with the FEM. This confirms again Theorem 4.1 and supports the discussions given in Section 4.2 in [1]. All the PIM methods have higher convergence rate compared with the FEM, except the linear ES-PIM that has about the same rate as the FEM. The numerical rates of convergence of PIM models in energy norm are in the range of 1.02–1.51 which is very close to the highest theoretical value of 1.5 measured in  $G^1$  norm given in Equation 86 in [1]. All the rates of convergence for the PIM models are higher than that of the FEM model of 0.97 whose theoretical value is 1.0. In terms of convergence rate, quadratic ES-PIM (1.51) and ES-RPIM (1.4) outperform the rest. This may partially be attributed to the higher-order interpolation

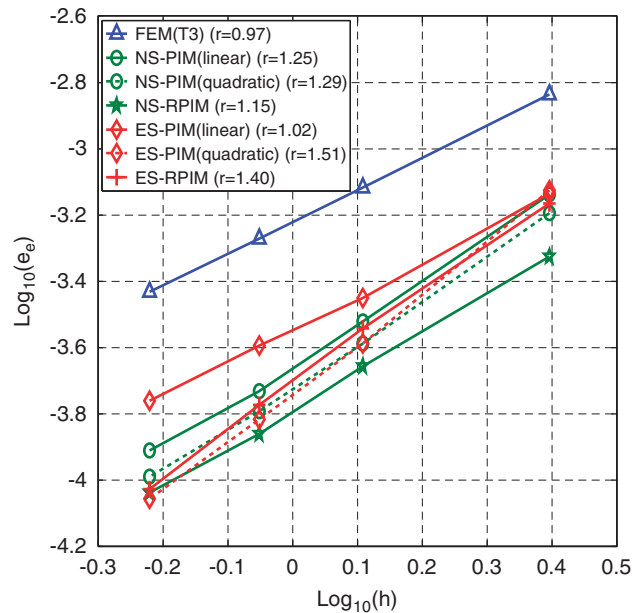


Figure 11. Convergence of the solutions in strain energy norm for the cantilever solved using different methods and the same set of irregular triangular mesh. All the PIM methods have much higher accuracy compared with the FEM. All the PIM methods have higher convergence rate compared with the FEM, except the linear ES-PIM that has about the same rate as the FEM. In terms of convergence rate, the ES-RPIM outperforms; and in terms of the accuracy the NS-RPIM stands out and is about 8 times more accurate than the FEM. In the energy norm measure the quadratic PIMs perform better than their linear counterpart, although it is not that significant.

used. In terms of accuracy all of the PIM family performs extremely well, and the accuracy is about 2–4 times greater than the FEM in terms of energy norm. This again reflects the theoretical discussions given in Section 4.2 in [1]. We note that in linear FEM models, the convergence rate of the interpolation error in  $G^1$  norm is the same as the error in strain energy norm defined in Equation (41). For our  $W^2$  formulation, we can expect a similar relationship, but it has not been established theoretically. In terms of accuracy a NS-RPIM stands out and it is about 4 times more accurate than the FEM. In the energy norm measure the quadratic PIMs perform better than their linear counterpart, although it is not very significant.

Figure 12 shows the solutions converging to the exact solution for the cantilever problem obtained using different methods and the same set of irregular triangular mesh. First, we observe the fact that all the  $W^2$  PIM methods give upper bound solutions with respect to the FEM solution. This confirmed Remark 3.5 in [1] and Theorem 3.4 numerically. Second, except the linear ES-PIM, all the PIM methods give upper bound to the exact solutions, in contrast to the FEM model that gives the lower bound to the exact solution. This confirms again Theorem 4.1. Quadratic PIMs and RPIMs give tighter upper bounds. The pair of linear ES-PIM and quadratic ES-PIM provides both upper and lower bounds that are very tight for this problem. The outstanding performance of the edge-based smoothing methods was reported in great detail in the [6] in the FEM settings: ES-FEM.

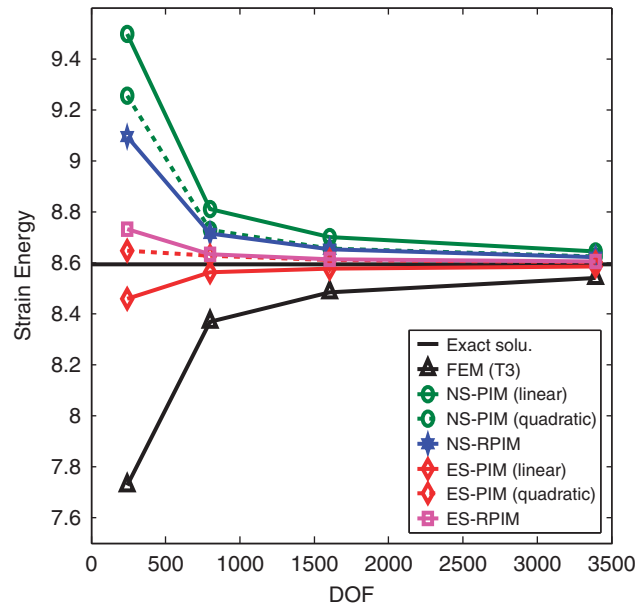


Figure 12. Solutions converging to the exact solution for the cantilever problem obtained using different methods and the same set of irregular triangular mesh. Except the linear ES-PIM, all the PIM methods give upper bound solutions in contrast to the FEM that gives the lower bound solution. Quadratic PIMs and RPIMs give tighter upper bounds. The pair of linear ES-PIM and the quadratic ES-PIM provide both upper and lower bounds that are very tight.

Figure 13 shows the solution in the maximum Von Mises stress at the node located at (0, 5) (upper-left corner) on the cantilever problem obtained using different methods and the same set of irregular triangular mesh. In all these models we perform the same ‘area-weighted averaging’ post-processing to get the stress at the node. From the analytic solution we know that the maximum Von Mises stress will occur at either the upper-left or the lower-left corners of the cantilever. The results of the numerical models have also detected the same and point to either of these two corners for all the models. From Figure 13 we found that the NS-PIMs give the best solution, followed by the ES-PIMs and FEM.

### 6.3. Rectangular plate with a crack

A rectangular plate ( $4a \times 2a$ ) with a crack of length  $a = 20$  shown in Figure 14(a) is analyzed using linear ES-PIM. The left edge of the plate is constrained, while the right side is subjected to horizontal unit traction. Plane stress problem is studied with the material parameters of  $E = 3.0 \times 10^7$  Pa and  $\nu = 0.3$ . Because of the presence of the crack, we expect stress singularity at the crack tip. A proper mesh is therefore needed, and the best way to obtain such a mesh is to conduct adaptive analysis. Since we can use triangular elements with ease in our models and mesh can be very irregular, an adaptive analysis can be performed easily using the local re-meshing technique presented in [24]. The refinement process takes 4 steps to complete, and the mesh at the 4th stage is as shown in Figure 14(b). with 1084 nodes. The energy error indicator is controlled within 5% in relation to the global total energy, and the details on the error estimation techniques can be found in [24].

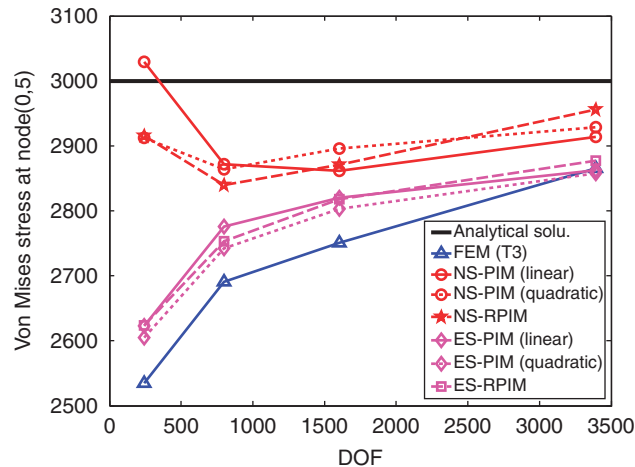


Figure 13. Solutions in the maximum Von Mises stress at the node located at (0, 5) (upper-left corner) on the cantilever problem obtained using different methods and the same set of irregular triangular mesh.

The results in terms of stresses are shown in Figure 14(c), and it is found that the results agree well with those obtained using EFG [15].

Note that a more proper modeling of problems with crack needs simulating the singular stress field. We are still working on the creation of such a singular field for the proposed models, and will present much more detailed formulations on the singular field creation and numerical results for this type of problems in the future. When the singular field is properly modeled, one needed only a very coarse mesh to obtained good solutions including the energy release rate.

#### 6.4. Application to a 3D axletree

Finally, to demonstrate our model on 3D problems, a 3D practical problem of axletree base is studied using one of the  $W^2$  methods: NS-PIM with linear interpolation. As shown in Figure 15, the axletree base is symmetric, fixed in the locations of four lower cylindrical holes and subjected to a uniform pressure ( $P = 1000 \text{ N/m}^2$ ) applied on the concave cricoid surface and fixed along the surface of four cylindrical holes. The material constants are taken as  $E = 3.0 \times 10^7 \text{ Pa}$  and  $\nu = 0.3$ .

The analysis was done using NS-PIM with 21 340 4-node tetrahedron elements and 4859 nodes. The contour of the Von Mises stress is shown in Figure 16. The maximum Von Mises stress is found as 6.607 kPa. A reference solution for comparison is also obtained using a very fine FEM model with 30 916 nodes which has about 7 times more nodes than the NS-PIM model. The maximum Von Mises stress of the very fine FEM model is found as 6.765 kPa. The difference between the coarse NS-PIM and the very fine FEM model in the maximum Von Mises stress is about 2%.

#### 6.5. Issues on computational efficiency: a comparative study

To conduct a meaningful and fair test on the computational efficiency of these numerical methods, we choose the problem of a square plate. This is because the exact solution for this problem is not in a simple polynomial form and hence allows us to use many nodes without getting too fast the

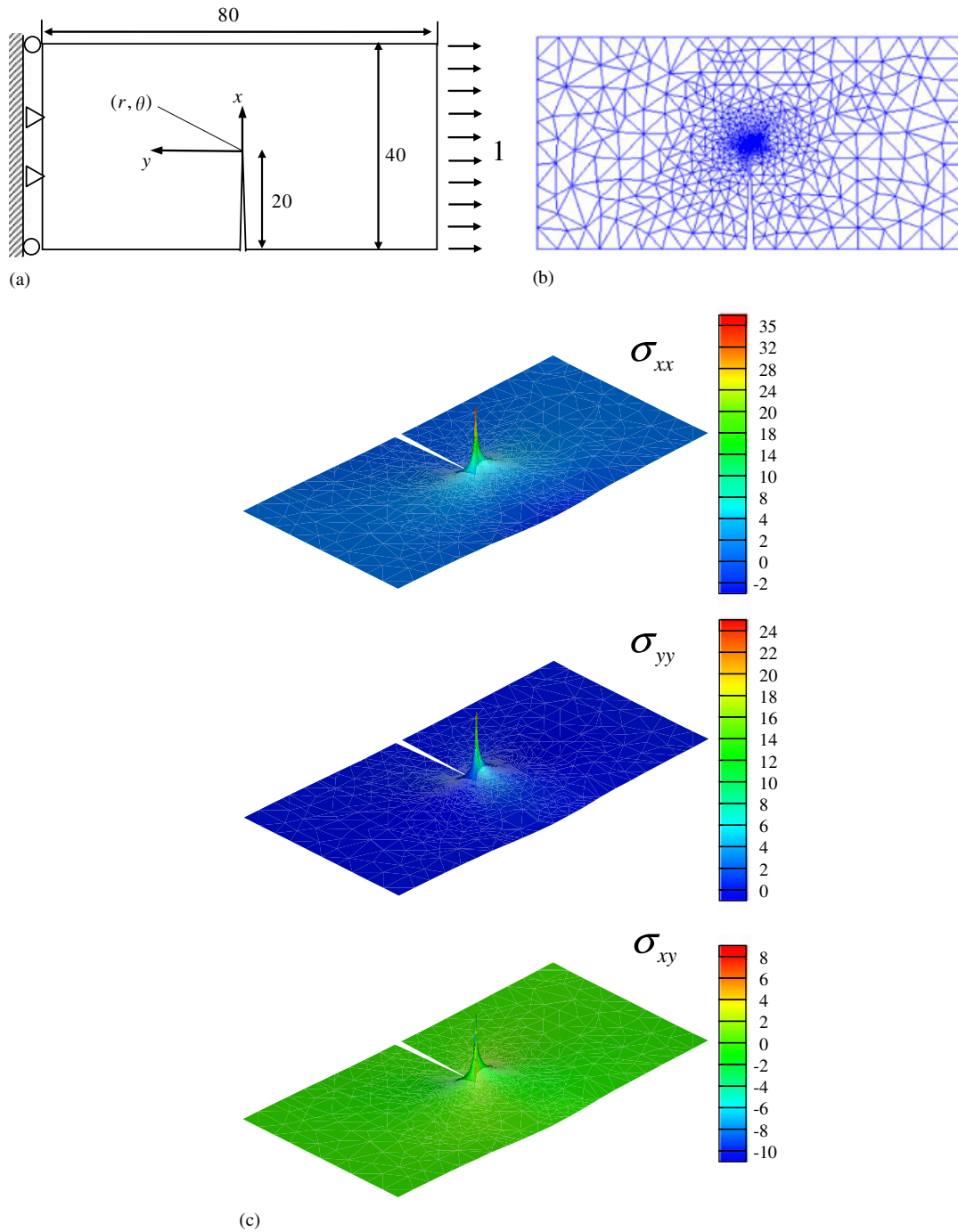


Figure 14. Stress distribution in an L-plate obtained using the linear ES-PIM.

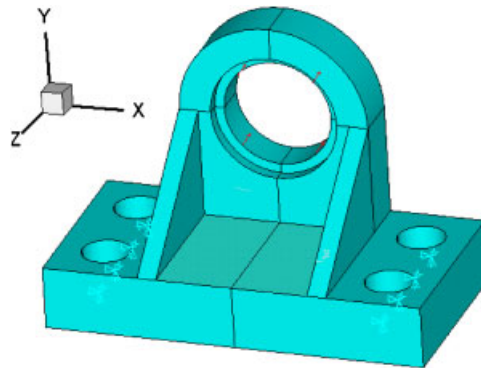


Figure 15. A 3D axletree base.

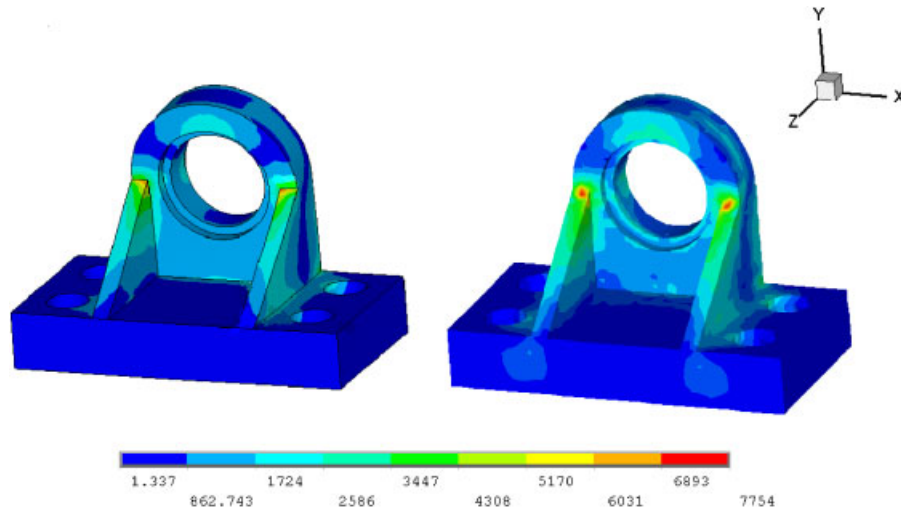


Figure 16. The contour of the Von Mises stress distribution. On the left: reference solution obtained using FEM with 30916 nodes; On the right obtained using NS-PIM with 21 340 4-node tetrahedron elements (4859 nodes).

exact solution. In addition, we have the exact solution to quantify the error accurately. The plate is of 10 m multi 10 m with a central circular hole of 1 m subjected to a unidirectional tensile load of  $10.0\text{N/m}^2$  in the  $x$  direction. The martial constants are  $E = 1.0 \times 10^3 \text{ Pa}$ ,  $\nu = 0.3$ . The detailed settings of the problem can be found in [2], and exact solution can be found in [23].

**6.5.1. Overhead cost.** The computational cost of a model consists of two parts: ‘overhead’ costs for all operations until the stiffness matrix is formed (including Gauss integration, etc.), and the solver time to solve the resultant system equations. In our  $W^2$  models, the overhead time includes the smoothing operations. On the one hand, they require computation that the FEM does not. On

Table II. Comparison of the CPU time (s) for different methods (3-node triangular mesh with 22 930 nodes).

Methods	FEM	ES-PIM	NS-PIM
Overhead	2.19	2.33	2.20
Solver	24.64	77.82	103.6
Total	26.83	80.15	105.8
Ratio	1.0	2.99	3.94

the other hand, it saves time for the computation of the derivatives of the shape functions that are needed in the FEM for domain-type Gauss integration (if the elements are not linear triangles). Therefore, overall it should not have too much difference. To confirm this we conducted a detail analysis of all linear models. The results for the overhead costs are listed in Table II. The tests are conducted on a Dell PC of Intel<sup>®</sup> Pentium(R) CPU 2.80 GHz, 1.00 GB of RAM. In the test, FEM, ES-PIM, and NS-PIM all use exactly the same triangular mesh. It is clear that there is not much difference in the overhead computations for all these three models. Note that the linear FEM of triangular elements requires the least overhead time among all the FEM models of other types of elements, because the computation of the derivatives of linear shape functions is trivial (constant) and the integration is also very simple (elemental summation). The linear ES-PIM and NS-PIM are as efficient as the linear FEM in terms of overhead costs. Most meshfree methods, however, will surely lose out to FEM in this regard [15].

*6.5.2. Solver cost for same mesh.* Note that the major cost in a computation of a not-too-small model is solving the system equations, and therefore we need to further examine the solver CPU time for these methods. Such a test will of course depend on the type of solver used. In the PIM models, there is no increase in degrees of freedoms, compared with the FEM model using the same mesh. If a full matrix solver is used the CPU time for PIMs should be the same as the FEM model using the same mesh. Because the solutions of PIMs are more accurate than that of the FEM, the computational efficiency of PIMs will be surely higher than the FEM, as discussed in [2]. In this work, we have just conducted a test using a very efficient bandwidth solver coded in MFree2D<sup>®</sup>, and the results are also listed in Table II. It is clear that the meshfree type methods consume more CPU time: ES-PIM is about 3 times and NS-PIM is about 4 times that of FEM. It is found that these meshfree type of methods are comparable to FEM methods, although they are still slower than the FEM model using the same set of nodes. Note that many other widely used meshfree methods need about 20–50 times CPU time compared with FEM. We also note that the solver time is much more (10 to 50 times) than the overhead time. This means that the overhead time is negligible which is a well-known fact in FEM analysis.

*6.5.3. Computational efficiency.* A fair comparison should be the *computational efficiency*: total (overhead + solver) CPU time needed for obtaining the results of the same accuracy. An efficiency test is therefore conducted, and the results are listed in Table III for the error in displacement norm. It is found that the ES-PIM is about 8 times more efficient than the FEM. However, the NS-PIM is about 3 times less efficient than the FEM, showing that obtaining an upper bound solution is more costly. Table IV shows the error in energy norm defined in Equation (39). It is found that

Table III. Computational efficiency: total CPU time needed for obtaining the results of the same accuracy in displacement norm (for error in displacement solutions at  $e_d = 1.0E-4$ ).

Methods	FEM-T3	ES-PIM-T3	NS-PIM-T3
Total CPU time (s)	92.4	11.1	270.6
Ratio	1.0	$\frac{1}{8.33}$	$\frac{1}{0.34}$

Table IV. Computational efficiency: total CPU time needed for obtaining the results of the same accuracy in energy norm (for error in energy solutions at  $e_e = 6.31E-7$ ).

Methods	FEM-T3	ES-PIM-T3	NS-PIM-T3
Total CPU time (s)	547.7	12.6	23.3
Ratio	1.0	$\frac{1}{43.4}$	$\frac{1}{23.5}$

the ES-PIM is as much as 40 times more efficient than the FEM, and even the NS-PIM is about 20 times more efficient than the FEM for this test.

## 7. CONCLUSION

In this paper we have established for the first time the  $G^1$  spaces with a set of important inequalities, based on which a weakened weak ( $W^2$ ) formulation has been proposed with necessary theories ensuring the stability and convergence of the formulation. A number of example problems are used to examine the  $W^2$  models confirming our theoretical predications. Compared with a standard weakform model that searches for solution in a proper  $H^1$  space, the  $W^2$  model searches for solutions in a proper  $G^1$  space, which leads to the following major significances:

1.  $W^2$  formulation is a unified formulation for all the compatible and incompatible models, thanks to the newly established  $G$  space theory. It works well for settings of the finite element methods (FEM) and meshfree methods.
2. Much more flexible ways of shape function construction can now be used: one does not need to worry too much about the compatibility of the assumed displacement functions, all one needs is the linear independence of the shape functions.
3. We can now search for solution from both sides (below and above) in proper  $G^1$  spaces. This offers the possibility for use to obtain both lower and upper bound solutions, ultra-accurate solutions, and even 'exact' solutions.
4. The numerical model created becomes softer, which offers a very much needed relief on the overly stiff phenomenon in the standard FEM models.
5. The  $W^2$  models work well with triangular meshes, which relieves the burden on creation quality meshes for complicated geometries.
6. The linear ES-PIM is about 8 times more efficient in displacement norm and 40 times in energy norm than the FEM for the test problem of the plate with a hole. The linear ES-PIM

gives a lower bound (for all the problems analyzed so far in Liu's group), but very accurate solution.

7. The linear NS-PIM is found to be about 3 times less efficient than the linear FEM, but it can offer important upper bound solutions for problems with complicated geometry.

#### ACKNOWLEDGEMENTS

The author would like to thank Dr Zhang GY for his help in the running of these example problems for this paper. Thanks are extended to Dr Xu X, Mr T. Nguyen-Thoi, Dr H. Nguyen-Xuan, Mr Cheng Lei and many other members at ACES for their comments and suggestions for this work. This work is partially supported by A\*STAR, Singapore. It is also partially supported by the Open Research Fund Program of the State Key Laboratory of Advanced Technology of Design and Manufacturing for Vehicle Body, Hunan University, People's Republic of China under the grant number 40915001.

#### REFERENCES

1. Liu GR. A G space theory and a weakened weak ( $W^2$ ) form for a unified formulation of compatible and incompatible methods: part I theory. *International Journal for Numerical Methods in Engineering* 2009; DOI: 10.1002/nme.2719.
2. Liu GR, Zhang GY, Dai KY, Wang YY, Zhong ZH, Li GY, Han X. A linearly conforming point interpolation method (LC-PIM) for 2D mechanics problems. *International Journal of Computational Methods* 2005; **2**: 645–665.
3. Zhang GY, Liu GR, Wang YY, Huang HT, Zhong ZH, Li GY, Han X. A linearly conforming point interpolation method (LC-PIM) for three-dimensional elasticity problems. *International Journal for Numerical Methods in Engineering* 2007; **72**:1524–1543.
4. Zhang GY, Liu GR, Nguyen TT, Song CX, Han X, Zhong ZH, Li GY. The upper bound property for solid mechanics of the linearly conforming radial point interpolation method (LC-RPIM). *International Journal of Computational Methods* 2007; **4**(3):521–541.
5. Liu GR, Nguyen TT, Nguyen XH, Lam KY. A node-based smoothed finite element method (N-SFEM) for upper bound solutions to solid mechanics problems. *Computers and Structures* 2009; **87**:14–26.
6. Liu GR, Nguyen TT, Lam KY. An edge-based smoothed finite element method (E-SFEM) for static and dynamic problems of solid mechanics. *Journal of Sound and Vibration* 2009; **320**:1100–1130.
7. Nguyen TT, Liu GR, Lam KY, GY Zhang. A face-based smoothed finite element method (F-SFEM) for 3D linear and nonlinear solid mechanics problems using 4-node tetrahedral elements. *International Journal for Numerical Methods in Engineering* 2008; DOI: 10.1002/nme.2491.
8. Liu GR, Nguyen TT, Dai KY, Lam KY. Theoretical aspects of the smoothed finite element method (SFEM). *International Journal for Numerical Methods in Engineering* 2007; **71**:902–930.
9. Liu GR, Li Y, Dai KY, Luan MT, Xue W. A Linearly conforming radial point interpolation method for solid mechanics problems. *International Journal of Computational Methods* 2006; **3**:401–428.
10. Liu GR. A generalized gradient smoothing technique and the smoothed bilinear form for galerkin formulation of a wide class of computational methods. *International Journal of Computational Methods* 2008; **5**(2):199–236.
11. Hughes TJR. *The Finite Element Method*. Prentice-Hall: London, 1987.
12. Belytschko T, Lu YY, Gu L. Element-free Galerkin methods. *International Journal for Numerical Methods in Engineering* 1994; **37**:229–256.
13. Liu GR. On a G space theory. *International Journal of Computational Methods* 2009; **6**(2):257–289.
14. Liu GR, Zhang GY. Upper bound solution to elasticity problems: a unique property of the linearly conforming point interpolation method (LC-PIM). *International Journal for Numerical Methods in Engineering* 2008; **74**:1128–1161.
15. Liu GR. *Meshfree Methods: Moving Beyond the Finite Element Method* (2nd edn). CRC Press: Boca Raton, U.S.A., 2009.
16. Liu GR, Dai KY, Nguyen TT. A smoothed finite element method for mechanics problems. *Computational Mechanics* 2007; **39**:859–877.
17. Dai KY, Liu GR, Nguyen TT. An  $n$ -sided polygonal smoothed finite element method (nSFEM) for solid mechanics. *Finite Elements in Analysis and Design* 2007; **43**:847–860.

18. Liu GR, Quek SS. *Finite Element Method: A Practical Course*. Butterworth-Heinemann: Burlington, MA, 2003.
19. Liu GR, Zhang GY. Edge-based smoothed point interpolation method (ES-PIM). *International Journal of Computational Methods* 2008; **5**(4):621–646.
20. Liu GR, Zhang GY. A normed G space and weakened weak ( $W^2$ ) formulation of a cell-based smoothed point interpolation method. *International Journal of Computational Methods* 2009; **6**(1):147–179.
21. Chen JS, Wu CT, Yoon S, You Y. A stabilized conforming nodal integration for Galerkin mesh-free methods. *International Journal for Numerical Methods in Engineering* 2001; **50**:435–466.
22. Liu GR, Gu YT. *An Introduction to MFree Methods and their Programming*. Springer: Berlin, 2005.
23. Timoshenko SP, Goodier JN. *Theory of Elasticity* (3rd edn). McGraw-Hill: New York, 1970.
24. Liu GR, Tu ZH. An adaptive procedure based on background cells for Meshfree methods. *Computer Methods in Applied Mechanics and Engineering* 2002; **191**:1923–1943.